Applied Catalysis B: Environmental 219 (2017) 479–491

Contents lists available at ScienceDirect

Applied Catalysis B: Environmental

journal homepage: www.elsevier.com/locate/apcatb

Research paper

Dibenzothiophene hydrodesulfurization with NiMo and CoMo catalysts supported on niobium-modified MCM-41

Franklin J. Méndez[a,*], Oscar E. Franco-López[a], Xim Bokhimi[b], Dora A. Solís-Casados[c], Luis Escobar-Alarcón[d], Tatiana E. Klimova[a,*]

[a] Facultad de Química, Universidad Nacional Autónoma de México (UNAM), Ciudad Universitaria, Coyoacán, Ciudad de México 04510, Mexico
[b] Instituto de Física, Universidad Nacional Autónoma de México (UNAM), Apartado Postal 20-364, Ciudad de México 01000, Mexico
[c] Centro Conjunto de Investigación en Química Sustentable, Universidad Autónoma del Estado de México-Universidad Nacional Autónoma de México (UAEM-UNAM), Km 14.5 Carretera Toluca-Atlacomulco, Unidad San Cayetano, Toluca, Estado de México 50200, Mexico
[d] Departamento de Física, Instituto Nacional de Investigaciones Nucleares (ININ), Apartado Postal 18-1027, Ciudad de México 11801, Mexico

ARTICLE INFO

Article history:
Received 3 February 2017
Received in revised form 31 May 2017
Accepted 26 July 2017
Available online 28 July 2017

Keywords:
Niobium
CoMo catalysts
NiMo catalysts
MCM-41
Hydrodesulfurization

ABSTRACT

In the present work, we studied the effect of the addition of niobium to CoMo/MCM-41 and NiMo/MCM-41 catalysts on their characteristics and performance in the hydrodesulfurization of dibenzothiophene. The MCM-41 support was synthesized at room temperature according to a well-known procedure. The metal species (Nb, Mo, Ni or Co) were deposited by successive impregnation using aqueous solutions of the corresponding metal salts. MCM-41 and Nb-containing MCM-41 supports were characterized by X-ray diffraction, N_2 physisorption, FT-Raman spectroscopy, X-ray photoelectron spectroscopy, UV–vis diffuse reflectance spectroscopy and scanning electron microscopy. The CoMo and NiMo catalysts in oxide state, in addition to the above techniques, were characterized by temperature-programmed reduction and the sulfided catalysts were characterized by high resolution transmission electron microscopy. The results show that the incorporation of small amounts of Nb (3–5 wt.%) increased the catalytic activity of both NiMo and CoMo catalysts in dibenzothiophene hydrodesulfurization and affected their selectivity. The effect of Nb on the selectivities of the NiMo and CoMo catalysts was different: for the NiMo catalysts, Nb increased selectivity towards the HYD route, whereas for the CoMo catalysts, it increased selectivity towards the DDS route. The analysis of the effect of Nb on the catalysts' selectivity was performed based on the kinetic constants calculated for the different steps of the DBT HDS network.

1. Introduction

In the last few years, the world community has decided to lower sulfur content in petroleum-derived fossil fuels. In many countries, petroleum-derived diesel fuel should have less than 50 ppm of S or even lower sulfur content (below 10 ppm) [1–3]. The hydrodesulfurization (HDS) process is one the most important processes used in a refinery to remove sulfur-containing aromatic compounds such as thiophenes, benzothiophenes, dibenzothiophenes and their alkyl-substituted derivatives from petroleum fractions [4–6]. At the industrial level, this reaction is carried out in fixed bed reactors at a temperature range from 300 to 400 °C and hydrogen pressure from 3 to 13 MPa. The common catalysts used for removal of sulfur from heavy oil fractions consist mainly of an Al_2O_3-supported MoS_2 active phase promoted with Co or Ni. The promoter's role is the modification of the electronic properties of the active phase and improvement of its dispersion, thus enhancing the catalytic activity in sulfur elimination. It is generally thought that catalytically active sites are sulfur vacancies associated with Mo atoms located on the edge surface of MoS_2 crystallites. The catalytic properties of these sites strongly depend on the neighboring promoter atoms of Co or Ni in the so-called Co(Ni)-Mo-S structures [6].

In order to obtain the currently required sulfur levels, it is necessary to increase the severity of the hydrotreatment process (perform it at a higher hydrogen pressure and temperature), increase the reactor volume, etc., which means a strong investment in the development of new HDS capacities. To do this in the most efficient and economic way is a major challenge for the refiners, catalyst manufacturers and process designers.

Mesoporous MCM-41 has been the focus of much research interest since its discovery in 1992 because it offers a uniform pore size between 15–100 Å and a high specific surface area (~1000 m^2/g) [7]. Mesoporous MCM-41 is an interesting option as a catalytic

* Corresponding authors.
E-mail addresses: frankmendez.mz@gmail.com (F.J. Méndez), klimova@unam.mx, tklimova@gmail.com (T.E. Klimova).

http://dx.doi.org/10.1016/j.apcatb.2017.07.079
0926-3373/

support for different applications. MCM-41 has been investigated, giving promising results for HDS reactions [8–18]. In the literature, there is evidence that the performance of supported catalysts depends not only on the high surface area of the support, but also is related to the support's surface properties, which can be modified during the preparation procedure or by the addition of some additives to the support.

Among many different materials, niobium-containing solids have attracted special attention in the field of heterogeneous catalysis. Probably, this is due to a versatility of possible applications of niobium species in catalysis, namely, they can be used as active phases, supports or promoters [19]. It was found that Nb-containing materials are effective supports and catalysts for liquid and gas phase oxidation processes [20], selective oxidation [21–23], epoxidation [24,25], hydrogenation [26,27] and photocatalysis [28] among other important catalytic reactions. It was observed that niobium could modify adsorption and catalytic properties when added to metal oxide catalysts or supports. In addition to the above mentioned catalytic applications of Nb-containing catalysts, it was also tested as an active phase for HDS. Among the advantages of this active phase, low cost and moderate acidity can be mentioned [29–35]. Previous reports indicated that in the unsupported state, niobium sulfide exhibits better activity than bulk molybdenum sulfide in the hydrotreatment of certain model compounds [36]. In addition, sulfided niobium catalysts supported on alumina or carbon showed higher activities in thiophene HDS than the reference MoS_2/Al_2O_3 catalyst [30,31]. Likewise, in work [35], a positive effect of the addition of niobia to the alumina support on both hydrodesulfurization and hydrodenitrogenation activities of NiMo catalysts was observed. In this case, the enhanced catalytic performance was attributed to the increase in acidity of the support's surface. In the very recent work [37], Nb-modified mesoporous SBA-15 and HMS materials have been used as supports for NiMo HDS catalysts. However, in the latter work the focus was on the effect of the addition of thioglycolic acid at different steps of the catalyst preparation, whereas the effect of niobium in the support was not discussed.

Given the interesting properties of Nb-modified catalysts, the purpose of the present study was to evaluate the viability of the use of Nb-modified MCM-41 materials as supports for CoMo and NiMo catalysts and to determine the effect of Nb on their catalytic performance in the hydrodesulfurization of dibenzothiophene.

2. Experimental

2.1. Synthesis of MCM-41

The MCM-41 silica support was synthesized according to a previously published procedure [18]. In a typical synthesis, the aqueous precursor's gel was synthesized using a sodium silicate solution (Na_2SiO_3) prepared by the reaction between sodium hydroxide (NaOH, ≥97.0%, Reactivo Química Meyer) and fumed silicon oxide (SiO_2, particle size = 0.2–0.3 μm, surface area = 200 ± 35 m^2/g, Sigma-Aldrich) followed by their addition on an aqueous micelar mixture based on tetraethylammonium hydroxide (TEAOH, 20% in H_2O, Sigma-Aldrich) and cetyltrimethylammonium bromide (CTMAB, ≥98%, Sigma-Aldrich). The molar composition of the final gel was Na_2SiO_3 = 1 (formed from NaOH = 2 and SiO_2 = 1), TEAOH = 0.2, CTMAB = 0.25 and H_2O = 40. The alkalinity of the clear solution was decreased by the dropwise addition of diluted sulfuric acid (H_2SO_4, 95–98.0%, J.T. Baker Chemicals), until the pH reached a value between 9 and 10, keeping the mixture under magnetic stirring for 2 h. The resulting mixture was aged at room temperature for 24 h without stirring. Then, the obtained solid was separated by vacuum filtration and washed several times with distilled water. After drying at room temperature for 12 h, it was pulverized to fine particles. For the calcination procedure, the temperature was increased from room temperature to 550 °C at a linear rate of 1 °C/min, which was held for 8 h.

2.2. Preparation of NiMoxNbM and CoMoxNbM catalysts

The Ni(Co)Mo*x*Nb/MCM-41 catalysts were prepared by successive impregnation using an excess volume of precursors' aqueous solutions. The ammonium niobate(V) oxalate hydrate ($NH_4[NbO(C_2O_4)_2(H_2O)](H_2O)_n$, 99.99%, Sigma-Aldrich) was introduced first. Prior to the preparation of the catalysts, Nb-containing supports were dried (100 °C, 6 h) and calcined (500 °C, 4 h) increasing the temperature at a linear rate of 1 °C/min. The Nb-loaded samples were impregnated with ammonium heptamolybdate tetrahydrate ($(NH_4)_6Mo_7O_{24}{\cdot}4H_2O$, 81–83% MoO_3 basis, Sigma-Aldrich) and cobalt(II) sulfate heptahydrate ($CoSO_4{\cdot}7H_2O$, ≥99%, Sigma-Aldrich) or nickel(II) sulfate hexahydrate ($NiSO_4{\cdot}6H_2O$, 99%, Sigma-Aldrich). After the impregnation of each metal, the catalysts were dried (100 °C, 6 h) and calcined (500 °C, 4 h). The nominal composition of the catalysts was 3 wt.% of NiO (or CoO) and 15 wt.% of MoO_3 that corresponds to a metal content of 2.4 wt.% for Ni (or Co) and 10 wt.% for Mo, respectively. This composition allows to obtain an atomic ratio of 0.28 Ni(Co)/(Ni(Co) + Mo), which is typical of the metal composition for industrial catalysts.

Prepared samples were denoted as M (for MCM-41 support); *x*NbM (for Nb-containing MCM-41 supports); CoMo*x*NbM or NiMo*x*NbM (for CoMo and NiMo catalysts), where *x* represents Nb loading in the mesoporous supports (*x* = 0, 3, 5 and 10 wt.%).

2.3. Support and catalysts characterization

2.3.1. X-ray diffraction

Small-angle (SA-) and wide-angle (WA-) powder XRD patterns were obtained using a Bruker D8 Advance diffractometer at room temperature and CuKα radiation (λ = 1.5406 Å). Crystalline phases observed in the obtained diffraction patterns were identified with the help of the Joint Committee on Powder Diffraction Standards-International Center of Diffraction Data (JCPDS-ICDD) library using Powder Diffraction File (PDF) card number [38].

2.3.2. Nitrogen physisorption

Textural characteristics were measured using a Micromeritics ASAP 2020 automatic analyzer at liquid N_2 temperature (−196 °C). Prior to the experiments, the samples were degassed overnight under vacuum at 270 °C. Specific surface areas were calculated by the Brunauer-Emmett-Teller method (S_{BET}), the total pore volume (V_p) was determined by N_2 adsorption at a relative pressure of 0.98 and pore diameter was determined from the adsorption branch of the isotherms by the Barrett-Joyner-Halenda method ($D_{ads\text{-}BJH}$).

2.3.3. Elemental analysis

Co (or Ni), Mo and Nb contents in the fresh samples were determined using Scanning Electron Microscopy coupled to Energy-Dispersive X-ray analyzer (SEM-EDX) using a Jeol 5900 LV microscope with Oxford ISIS microanalyzer. Before analysis, the sample was deposited on a carbon holder and evacuated at high vacuum.

2.3.4. Micro-Raman spectroscopy

Micro-Raman analysis was carried out using an HR LabRam800 system equipped with an Olympus BX40 confocal microscope. A Nd:YAG laser beam (532 nm) was focused by a 50 X microscope objective to ≈1 μm in diameter on the sample's surface. The power of the laser towards the sample was regulated by a neutral density filter (OD = 1) to prevent sample heating and structural changes induced in the sample. A cooled CCD camera was used to record

the spectra, usually averaged for 100 accumulations in order to improve the signal to noise ratio. All spectra were calibrated using the 521 cm^{-1} line of a silicon wafer.

2.3.5. X-ray photoelectron spectroscopy

XPS measurements were performed with a JEOL JPS-9200 instrument equipped with a Mg Kα radiation source (1253.6 eV). The spectrometer was operated at a pass energy of 10 eV with an X-ray power of 300 W. The base pressure in the analyzing chamber was maintained in the order of 1×10^{-8} mbar. The binding energy was determined using the carbon C (1s) line as a reference with binding energy of 284.6 eV. Quantification and deconvolution were performed using the Gaussian functions of the Origin 8.1 software.

2.3.6. Ultraviolet-visible diffuse reflectance spectroscopy

UV–vis DRS spectra of supports and catalysts were recorded on a Varian Cary 100 Conc. spectrophotometer equipped with a diffuse reflectance attachment. Polytetrafluoroethylene reference was used.

2.3.7. Temperature-programmed reduction

Prior to TPR analysis, the catalyst samples were pretreated at 400 °C for 2 h under static air and cooled down to room temperature. The data was recorded using a Micromeritics AutoChem II 2920 automatic analyzer equipped with a TCD detector with an H_2/Ar flow. The temperature was increased from ambient temperature (25 °C) to 1000 °C at a rate of 10 °C/min.

2.3.8. High resolution transmission electron microscopy

A Jeol 2010 microscope was used for the HRTEM characterization of the selected sulfided catalysts. Resolving power of this equipment was 1.9 Å. Before the analysis, the sulfided samples were dispersed in heptane in an ultrasonic bath, and a drop of this suspension was deposited on a carbon-coated grid. More than 300 crystallites were measured for the estimation of slab length and layer stacking distributions of MoS_2 particles in different catalysts.

The average slab lengths (L) and stacking numbers (N) were calculated according to Eq. (1). In this equation, M_i is the slab length or stacking layer number of a stacked MoS_2 unit, and x_i is the number of slabs or stacks in a certain range of length or stacking layer number [39].

$$L\ (or\ N) = \frac{\sum_{i=1}^{n}(x_i M_i)}{\sum_{i=1}^{n}(x_i)} \quad (1)$$

The average fraction of Mo atoms on the edge surface of the MoS_2 crystals (f_{Mo}) was used as an indicator of the active phase dispersion. The f_{Mo} value was determined using Eq. (2) [40], assuming that the MoS_2 crystals are perfect hexagons [41]. In Eq. (2), the numerator is the number of atoms in the active surface (Mo_{edge}) and the denominator is the total number of Mo atoms in the crystal (Mo_{total}); t = number of layers in the MoS_2 particles and n_i = number of Mo atoms in one edge, determined from the average length L as shown in Eq. (3).

$$f_{Mo} = \frac{Mo_{edge}}{Mo_{total}} = \frac{\sum_{i=1}^{t}(6n_i - 6)}{\sum_{i=1}^{t}\left(3n_i^2 - 3n_i + 1\right)} \quad (2)$$

$$n_i = \frac{L}{6.4} + 0.5 \quad (3)$$

2.4. Catalytic activity tests

The dibenzothiophene hydrodesulfurization tests were carried out in a batch reactor under the following reaction conditions: 300 °C temperature,7.3 MPa total pressure and 8 h reaction time. Before the catalytic activity tests, the catalysts were sulfided *ex situ* at atmospheric pressure upon the following conditions: 400 °C, 4 h, in a stream of 20 mL/min of a mixture of H_2S (15 vol.%)/H_2. The sulfided catalysts were transferred to a batch reactor in an inert atmosphere (Ar). Previously, the reactor was filled with 40 mL of dibenzothiophene solution in hexadecane with 0.032 mol/L DBT concentration.

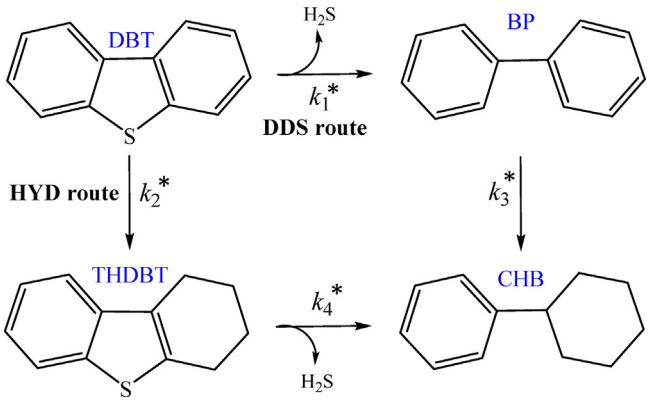

Scheme 1. Dibenzothiophene hydrodesulfurization reaction network used to calculate the catalytic constants based on the model proposed by H. Farag [42,43]. DBT = dibenzothiophene; THDBT = tetrahydrodibenzothiophene; BP = biphenyl; CHB = cyclohexylbenzene.

In order to characterize the hydrogenation (HYD route) and the direct desulfurization (DDS route) abilities of the catalysts, the composition of the reaction products was determined by taking samples of the reaction mixture every hour and analyzing them on an Agilent Technologies chromatograph, GC 6890 model, equipped with a flame ionization detector and 50 m length HP-1 capillary column. ChemStation Plus software was used for the integration of detected GC signals. Selectivity of the catalysts was characterized by their rate constants.

The kinetic constants were calculated based on the kinetic model proposed by H. Farag [42,43] for the reaction network shown in Scheme 1. This kinetic model is based on the assumption of the existence of two different kinds of catalytic active sites of (i) hydrogenation and (ii) direct desulfurization. In this approach, the total rate can be expressed as $R_{Total} = R_{HYD} + R_{DDS}$. The solved differential equations to calculate the catalytic constants are included in the Supplementary Information section. Five rate constants were calculated: k, overall pseudo-first-order rate constant; k_1^*, k_2^*, k_3^* and k_4^*, apparent rate constants, which were $k_n^* = k_n K_n$, where k_n is the intrinsic kinetic rate constant and K_n is the equilibrium adsorption constant of each compound. The overall rate constant $k = k_1^* + k_2^* = k_1 K_1 + k_2 K_2$, where k_1 and k_2 are the intrinsic kinetic rate constants for the DDS and HYD routes, and K_1 and K_2 are the equilibrium adsorption constants of DBT over the catalytic active sites for DDS and HYD, respectively. According to the Scheme 1, rate constants k_1^* and k_4^* are related to hydrogenolysis reactions (C—S bond cleavage), whereas k_2^* and k_3^* correspond to the hydrogenation of DBT and CHB, respectively. The kinetic equations were compiled until converged. For all the catalysts tested in this study, good fitting was obtained between the experimental points and the fitted curves based on the equations used to calculate catalytic constants involved in HDS of DBT reaction network.

3. Results and discussion

3.1. Support and oxide catalyst characterization

3.1.1. Small- and wide-angle X-ray diffraction

Fig. 1a and b show the small- (SA) and wide-angle (WA) diffractograms for the mesoporous materials used as catalyst supports. It

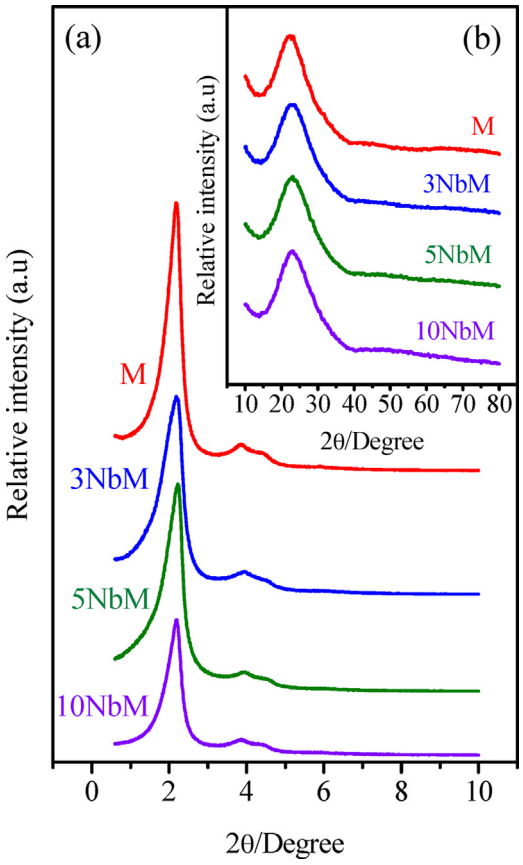

Fig. 1. (a) Small-angle and (b) wide-angle X-ray diffraction patterns of the prepared mesoporous supports.

can be seen that MCM-41 (denoted as "M") exhibited an intense reflection at 2θ = 2.2° and three weaker ones at 3.8°, 4.3° and 5.9° assigned to typical Bragg reflections (100), (110), (200) and (210), characteristic of high-quality hexagonal mesostructures with long-range 2D hexagonal arrangement of the channels and *p6mm* space group symmetry (Fig. 1a) [7]. Fig. 1a also shows the SA-XRD patterns of the niobium-modified MCM-41 mesoporous supports (denoted as "*x*NbM"). The highly ordered hexagonal pore structure of the MCM-41 was still preserved after Nb impregnation, meanwhile the relative intensities of the reflections characteristic of the MCM-41 were smaller for the *x*Nb/MCM-41 supports. This can be attributed to the modification of the MCM-41 pore walls with Nb_2O_5 species, which reduces the scattering contrast between the pores and the walls of the molecular sieve [44] or to some distortion of the long-range pore order. The structural parameters of the starting MCM-41 were not modified by Nb-incorporation, presenting approximate values of 40 (± 0.2 Å), 46 (± 0.2 Å) and 21 Å (± 1.7 Å) for basal interplanar spacing values (d_{100}), lattice parameter (a_0) and pore wall thickness (δ), respectively. On the other hand, WA-XRD patterns (Fig. 1b) of the parent MCM-41 showed a broad band in the range of 15–40° 2θ, which is characteristic of amorphous silica material [45]. Nb-containing MCM-41 supports showed similar diffractograms as of starting MCM-41 silica. No signals attributable to the presence of the Nb_2O_5 crystalline phase were detected, which points out the small crystallite size (less than 5 nm) or high dispersion of the deposited Nb(V) oxide species.

The diffractograms of the prepared NiMo and CoMo catalysts are shown in Fig. 2. Fig. 2a shows the SA-XRD patterns of the prepared NiMo catalysts. One main reflection can still be seen in these diffractograms at about 2.2° (2θ). However, the relative intensity of this signal for the catalysts was much smaller than that observed for the corresponding supports (Fig. 1a). In addition, instead of the other three weak signals which were observed for the supports at 3.8°, 4.3° and 5.9° (2θ), in the diffraction patterns of the catalysts only one small-intensity, poor-resolved signal can be seen at about 4° (2θ). The catalysts of a CoMo series showed similar behavior when their SA-XRD patterns (not shown) were compared to those of the corresponding supports. The above results indicate that even if the hexagonal pore arrangement of the MCM-41 and *x*Nb/MCM-41 supports was still maintained in the NiMo and CoMo catalysts, the long-range 2D hexagonal pore order in the catalysts was significantly affected by the incorporation of the metal oxide species. Probably, this can be due to the agglomeration of the deposited metal species inside the support's pores and on its external surface, leading to pore blockage, or to some destruction of the MCM-41-support structure during the impregnation of aqueous solutions of metal species upon heating. However, these assumptions need further experimental confirmation.

Fig. 2b and c show WA-XRD patterns of the prepared CoMo and NiMo catalysts, respectively. Similarly to WA-XRD patterns of the supports (Fig. 1b), the diffractograms of the fresh catalysts presented a broad peak between 15 and 40° (2θ) attributed to the amorphous silica of the MCM-41 support [45]. In addition to this broad peak, some small intensity signals can be seen in the diffraction patterns of some of the NiMo and CoMo catalysts. These signals were assigned to the presence of some crystalline phases of the Co (or Ni) and Mo oxide species. Thus, some mesoporous catalysts exhibited signals at 22.7° and 28.5° (2θ) which correspond to (110) and (220) reflections of the MoO_3 phase (PDF #76-1003). Another weak peak observed in the XRD patterns of the CoMo catalysts at 26.3°(2θ) can be assigned to the presence of some traces of the cobalt molybdenum oxide $CoMoO_4$ phase (PDF #21-0868). Although the small intensity of this signal and the absence of other signals of the above-mentioned crystalline phases did not allow us to make a more precise assignation, the appearance of this signal evidences that some agglomeration of cobalt oxide species took place in all prepared catalysts, independently on the support's Nb loading. For the catalysts of the NiMo series, a signal at 26.7° (2θ) was observed in the XRD patterns of the NiMo5NbM and NiMo10NbM catalysts that can be due to the (220) reflection of the $NiMoO_4$ crystalline phase (PDF #45-0142). It seems that the formation of these crystalline species was promoted on the MCM-41 supports modified with niobium at Nb loadings larger than 5 wt.%.

3.1.2. N_2 physisorption

MCM-41 prepared at room temperature (Supporting Information, Figs. S1a) presented a Type-IV isotherm, typical of a uniform mesoporous material, in agreement with the literature [18,46]. The N_2 adsorption-desorption isotherms of the *x*NbM supports (Fig. S1a), CoMo*x*NbM (Fig. S1b) and NiMo*x*NbM (Fig. S1c) catalysts were similar to that of the MCM-41 silica support. They had the same shape and the only difference observed was in the overall amount of adsorbed nitrogen, which was smaller than for the MCM-41 support. This can be ascribed to the increase in the materials' density due to the incorporation of Nb, Ni(Co) and Mo oxide species on the MCM-41 surface.

Table 1 shows the textural and structural characterization results of the prepared supports. When the textural characteristics of the starting MCM-41 (M) materials and Nb-containing MCM-41 supports (*x*NbM) are compared, it can be noted that the incorporation of Nb resulted in a significant decrease in the textural characteristics (S_{BET} and V_P). For example, when just 3 wt.% of Nb were incorporated in the MCM-41 material, the specific surface area of the support decreased from 1027 to 810 m^2/g (21% decrease), whereas the total pore volume changed from 1.06 to 0.78 cm^3/g (26% decrease). On one side, such a strong decrease in the textural characteristics of the MCM-41 material after Nb incor-

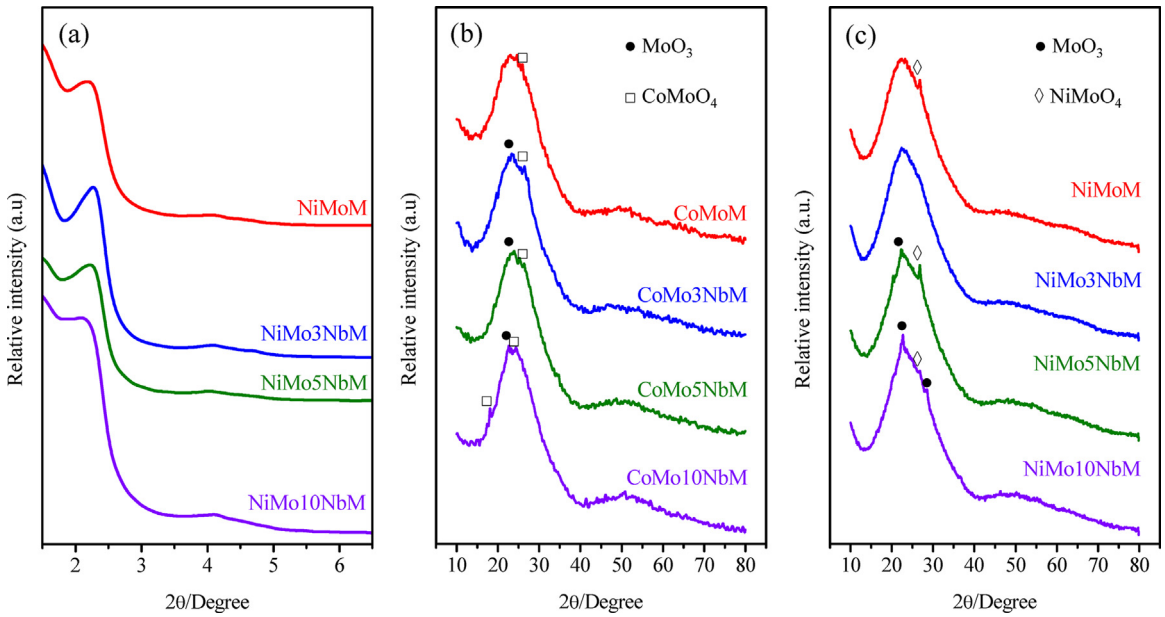

Fig. 2. Small-angle (a) and wide-angle X-ray diffraction patterns of the supported CoMo*x*NbM (b) and NiMo*x*NbM (c) catalysts, *x* represents supports' Nb loading (*x* = 0, 3, 5 and 10 wt.%).

Table 1
Structural and textural characteristics of the mesoporous supports.

Sample [a]	S_{BET} (m^2/g) [b]	V_p (cm^3/g) [c]	$D_{ads\text{-}BJH}$ (Å) [d]	d_{100} (Å) [e]	a_0 (Å) [f]	δ (Å) [g]
M	1027	1.06	25	40.7	47.0	22
M-T	854	0.85	26	38.2	44.1	18
3NbM	810	0.78	25	40.5	46.8	21
5NbM	758	0.71	27	40.1	46.3	18
10NbM	663	0.62	28	40.5	46.8	18

[a] M = MCM-41, M-T = water treated MCM-41 material; *x*NbM = *x*Nb/MCM-41, where *x* = 0, 3, 5 and 10 wt.% of Nb.
[b] Specific surface area determined by the BET method.
[c] Pore volume obtained at relative pressure of 0.98.
[d] Pore diameter determined from the adsorption branch of the isotherms by the BJH method.
[e] Basal interplanar spacing values (d_{100}).
[f] Lattice parameter (a_0) for a hexagonal pore structure: $a_0 = 2d_{100}/\sqrt{3}$.
[g] Pore wall thickness (δ) estimated as $\delta = a_0 - D_{ads\text{-}BJH}$.

poration can be ascribed to the agglomeration of the deposited Nb_2O_5 species. However, we think that another possible explanation can be ascribed to the preparation method used in the present work for the incorporation of niobium. Namely, the Nb(V) precursor salt was impregnated on the MCM-41 surface using an excess of the aqueous solution, and then the solvent (water) was evaporated upon heating of the above mixture on a magnetic stirrer. From the literature [47–49] it is known that the textural characteristics of silica-based mesoporous materials such as SBA-15, HMS and MCM-41, can be drastically affected by the exposure to water or even to air humidity during long-time storage. To prove this supposition, an additional experiment was performed in which the parent MCM-41 material was impregnated with the same amount of pure water (without Nb(V) precursor) following the same preparation method as described above. The obtained sample was denoted as "M-T" material, and its textural characteristics are also shown in Table 1, whereas its small-angle XRD pattern and nitrogen adsorption-desorption isotherm can be consulted in the Supporting Information section (Fig. S2). It can be seen that the water-treated M-T sample also showed a noticeable decrease in the specific surface area and pore volume (17 and 20 %, respectively), in addition to a small increase (~1 Å) in pore diameter and a decrease in pore wall thickness (~4 Å). Some dissolution of silica from the MCM-41 pore walls might have taken place in aqueous solutions upon heating. Therefore, the impregnation method used could also be partially responsible for the decrease in the textural characteristics of the *x*NbM samples. Similar instability of MCM-41 in aqueous solutions, especially at neutral and basic pH values, have been reported previously by Pham et al. [49]. This effect was also observed during the preparation of Nb-containing supports (Table 1), when Nb loading was varied between 3 and 10 wt.%, the average pore diameter increased from 25 to 28 Å, while the pore wall thickness decreased from 22 to 18 Å.

The textural characteristics of the synthesized CoMo and NiMo catalysts are shown in Table 2. It can be noted that the incorporation of the above-mentioned metal oxides on the M and *x*NbM supports resulted in a further decrease in the specific textural characteristics of the samples (S_{BET} and V_P). This decrease could be due to agglomeration of the deposited cobalt, nickel and molybdenum oxide species inside the mesoporous support pores that can cause pore plugging. This seems to be reasonable and in line with the powder WA-XRD characterization of the catalysts (Fig. 2b and c), where the formation of traces of crystalline MoO_3, $CoMoO_4$ and $NiMoO_4$ phases were detected. On the other side, a deterioration of the MCM-41 and *x*Nb/MCM-41 pore walls by the impregnation of aqueous solutions of metal precursors cannot be ruled out. In addition, Kumar-Rana and Viswanathan have suggested [50] that the thermal decomposition of the heptamolybdate precursor during calcination of the prepared Mo/MCM-41 catalysts can also cause a destruction of the MCM-41 pore-ordering.

Table 2
Textural characteristics and chemical composition of the prepared CoMo and NiMo catalysts.

Sample [a]	Textural properties [b]			Elemental composition (wt.%) [c]			Atomic ratio [d]	
	S_{BET} (m^2/g)	V_p (cm^3/g)	$D_{ads-BJH}$ (Å)	Co (Ni)	Mo	Nb	Ni(Co)/(Ni(Co)+Mo)	Nb/Mo
CoMoM	755	0.64	25	2.2	10.4	–	0.26	–
CoMo3NbM	630	0.55	26	2.1	9.8	3.6	0.26	0.4
CoMo5NbM	510	0.47	26	2.1	9.6	5.9	0.26	0.6
CoMo10NbM	479	0.44	25	2.3	10.6	10.4	0.26	1.0
NiMoM	713	0.76	25	2.2	10.7	–	0.27	–
NiMo3NbM	655	0.63	25	2.4	9.6	3.0	0.29	0.3
NiMo5NbM	522	0.52	26	2.0	10.6	5.3	0.26	0.5
NiMo10NbM	410	0.41	26	2.0	10.7	10.5	0.27	1.0

[a] CoMoxNbM = CoMoxNb/MCM-41; NiMoxNbM = NiMoxNb/MCM-41; where x = 0, 3, 5 and 10 wt.% of Nb.
[b] S_{BET}, specific surface area determined by the BET method; V_P, total pore volume obtained at relative pressure of 0.98; $D_{ads-BJH}$, pore diameter determined from the adsorption branch of the isotherms by the BJH method.
[c] Nominal composition of the catalysts: 2.4 wt.% of Co (or Ni) and 10 wt.% of Mo.
[d] Nominal atomic ratios: Ni(Co)/(Ni(Co) + Mo) = 0.28 and Nb/Mo = 0.0, 0.4, 0.6 and 1.0 for x = 0, 3, 5 and 10 wt.% of Nb, respectively.

3.1.3. Elemental analysis

The real metal contents in the prepared CoMo and NiMo catalysts supported on MCM-41 and xNb/MCM-41 materials were determined by SEM-EDX analysis (Table 2). It can be observed that the cobalt, nickel, molybdenum and niobium loadings in the mesoporous catalysts and their respective atomic ratios were close to the theoretically expected values.

3.1.4. FT-Raman spectroscopy

Raman spectra of pure silica MCM-41 (M) and Nb-containing MCM-41 supports (xNbM, where x = 3, 5 and 10 wt.%) are presented in Fig. 3. The spectrum of the bulk Nb_2O_5 obtained after the calcination of ammonium niobate(V) oxalate hydrate at 500 °C for 4 h in an air atmosphere is also shown for comparison purposes. In this spectrum, the following signals can be observed: a broad band centered at 673 cm^{-1}, a group of signals with maxima at about 192, 245 and 320 cm^{-1} and a low-intensity broad band at 916 cm^{-1}. According to literature [51,52], all these signals can be attributed to different vibration modes of crystalline Nb_2O_5. Thus, the first most intense signal (673 cm^{-1}) corresponds to symmetric stretching modes of octahedrally-coordinated NbO_6 structures. The second group of signals (between 350 and 170 cm^{-1}) is characteristic of bending modes of the Nb—O—Nb linkages. And, finally, the weak broad band at 916 cm^{-1} is due to the symmetric stretching mode of Nb=O surface sites of pentahedrally coordinated NbO_5 structures [52]. It should be mentioned that the tetrahedrally-coordinated structures (NbO_4) are rarely found in niobium oxide compounds, since the Nb^{5+} atom is too large to fit into an oxygen-anion tetrahedron [53].

The pure silica MCM-41 sample (M, Fig. 3) exhibits two Raman bands at 484 and 785 cm^{-1} assigned to the asymmetric and symmetric stretching vibrations of the Si—O—Si bonds, respectively. Other bands at 638 and 402 cm^{-1} are characteristic of the dehydrated amorphous silica surface [54], while the band at 976 cm^{-1} is associated with the stretching mode of vibrations of the surface silanol groups (—Si—OH) [55]. When the spectra of Nb-containing supports (3NbM, 5NbM and 10NbM) are compared to that of the starting MCM-41 sample, it can be noted that the intensity of the vibration mode ascribed to the Si—OH groups (976 cm^{-1}) decreases with increasing niobium content in the sample. This could be due to the interaction of surface silanol groups of MCM-41 with the deposited niobium oxide species. On the other hand, the most intense band of the bulk Nb_2O_5 (673 cm^{-1}) cannot be observed in the spectra of the 3NbM and 5NbM samples, suggesting that in these samples, there are no agglomerated Nb(V) oxide species and only highly-dispersed isolated niobium oxide species are present. A further increase in the Nb loading to 10 wt.% resulted in the almost complete disappearance of the silanol groups signal (976 cm^{-1}) and

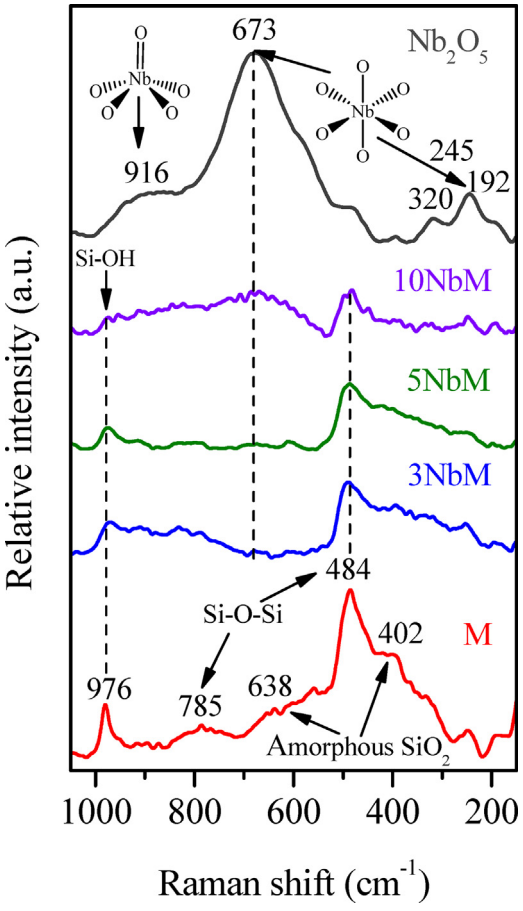

Fig. 3. Raman spectra of the prepared M and xNbM mesoporous supports with different Nb loadings (x = 0, 3, 5 and 10 wt.%). The spectrum of the bulk Nb_2O_5 obtained after the calcination of ammonium niobate(V) oxalate hydrate at 500 °C for 4 h is also included.

the appearance of a very low-intensity band at 673 cm^{-1}. It seems that at this Nb-charge, most of the Si—OH groups were transformed into Si—O—Nb ones due to the Nb grafting on the MCM-41 surface, and an excess of the deposited Nb(V) oxide formed some small Nb_2O_5 clusters or crystals not detectable by XRD.

3.1.5. X-ray photoelectron spectroscopy

M, xNbM and Nb_2O_5 materials were also characterized by XPS. Results obtained by this technique are shown in Fig. 4 and Table 3. XPS signals were assigned according to the official web page of National Institute of Standards and Technology (NIST) [56].

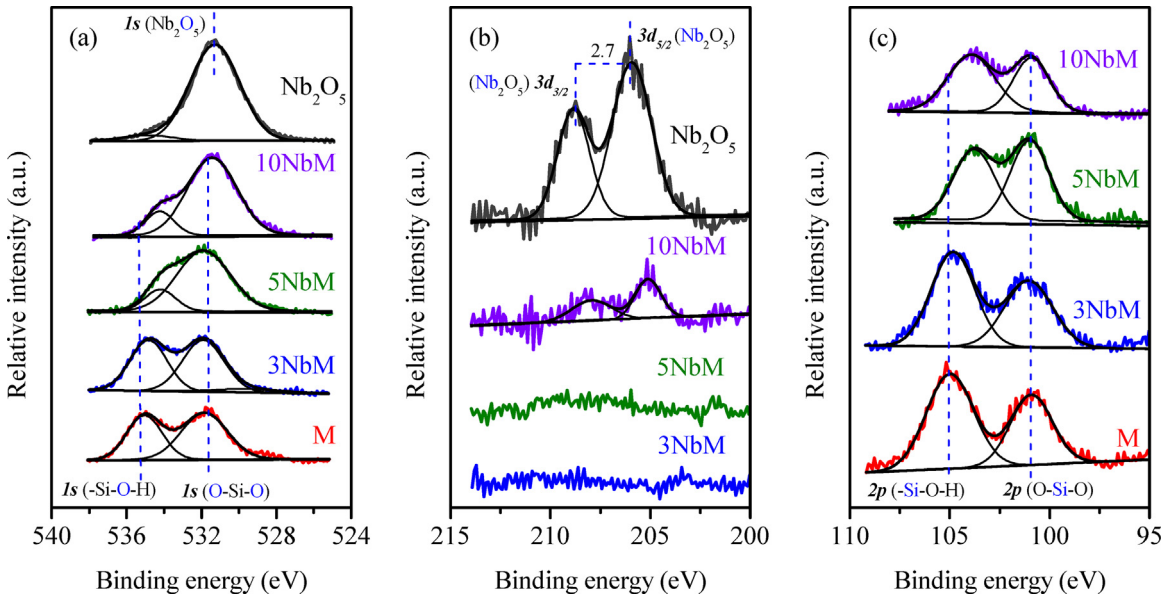

Fig. 4. Deconvoluted XPS spectra of mesoporous supports in (a) O1s, (b) Nb3d and (c) Si2p regions. The spectra of the bulk Nb_2O_5 obtained after the calcination of ammonium niobate(V) oxalate hydrate at 500 °C for 4 h are also shown in charts (a) and (b) for comparison purposes.

Table 3
Surface atomic concentrations of the O1 s species as determined by XPS elemental analysis.

Sample	Tetrahedral SiO_4	Silanol groups (Si-OH)	Ratio SiO_4/Si-OH
M	55.7	44.3	1.4
3NbM	57.8	42.2	1.3
5NbM	83.2	16.8	4.9
10NbM	84.9	15.1	5.6

The peaks' deconvolution revealed two distinct O1s (Fig. 4a) and Si2p (Fig. 4c) binding energy signals, indicating the existence of two different species. The first Si2p characteristic band corresponding to O—Si—O of tetrahedral SiO_4 species of silica was observed at about 101.0 eV (±0.1) (Fig. 4c). This band is consistent with the O1 s signal observed at about 531.6 eV that corresponds to the oxygen of SiO_4 species (O—Si—O, Fig. 4a). Another Si2p signal with the maximum between 105.3–103.9 eV (Fig. 4c) and a second O1s peak centered at 535.1–534.1 eV (Fig. 4a) can be ascribed to the surface silanol species (—Si—O—H). A progressive decrease in the relative intensity of the Si2p and O1s signals attributed to the silanol groups and a shift to lower binding energies can be observed with the increasing Nb loading in the supports. This could be related to the grafting of Nb(V) species on the hydroxyl groups of the MCM-41 support, in which surface —Si—O—H groups are transformed into the —Si—O—Nb ones. This assumption was confirmed by the calculation of the ratio of the intensities of O1s signals of the SiO_4/Si-OH types for the *x*NbM supports with different Nb loadings (Table 3). It was found that the above ratio increased with Nb loading from 1.4 for the M support to 5.6 for the 10NbM one. Therefore, results from both FT-Raman and XPS suggest that the Nb species were attached to the MCM-41 surface through the interaction with the silanol groups.

The X-ray photoelectron spectrum of the bulk Nb_2O_5 obtained after the thermal treatments of ammonium niobate(V) oxalate hydrate (500 °C, 4 h) revealed the presence of a well-resolved doublet with signals at 206.1 eV ($3d_{5/2}$) and 208.8 eV ($3d_{3/2}$) (Fig. 4b). The separation of 2.7 eV between the above-mentioned peaks correspond to Nb^{5+} in an oxide environment (Nb_2O_5). This assignation is corroborated by a symmetric peak in the O1s region centered at about 531.3 eV (Fig. 4a). No binding energy peaks of Nb3d were observed in the spectra of the 3NbM and 5NbM samples, probably because of low niobium content. However, in the spectrum of the 10NbM sample, Nb3d signals could be observed. They were slightly shifted to lower binding energy values compared to the signals of the bulk Nb_2O_5, probably due to the interaction with the MCM-41 silica support.

3.1.6. *UV–vis diffuse reflectance spectroscopy*

A UV–vis DRS characterization of the prepared supports and catalysts was performed to obtain more information about the coordination and aggregation state of the deposited Co (or Ni), Mo and Nb oxide species. The MCM-41 DR spectrum does not exhibit any absorption band (Fig. 5a), indicating that this material does not absorb UV or visible light. However, the bulk Nb_2O_5 obtained after the thermal treatments of ammonium niobate(V) oxalate hydrate at 500 °C for 4 h presented a broad band with the maximum at about 325 nm that is produced by the ligand-to-metal charge transfer (LMCT) $O^{2-} \rightarrow Nb^{5+}$ in octahedral coordination. In the spectra of the *x*NbM samples, main signals were observed at about 242, 246 and 250 nm for the Nb loadings of 3, 5 and 10 wt.%, respectively, which was significantly different from the position of the main signal of the bulk Nb(V) oxide (325 nm). As previously reported by Ziolek and Sobczak [57], the absorption signals of the *x*NbM samples can also be produced by LMCT in Nb(V) oxide species, but these species should be pentahedrally-coordinated as Nb(V) linked to a silica surface or they can have octahedral coordination, but high dispersion. A slight shift of the peak maximum from 242 nm to 250 nm with an increase in the Nb loading from 3 to 10 wt.% can be related to an increase in the degree of agglomeration of the deposited Nb(V) oxide species. These results are in line with the above described Raman results for the *x*NbM supports (Fig. 3).

Mo^{6+} has a d^0 electronic configuration, and therefore, the absorption bands in the UV–vis DR spectra of the Mo-based catalysts are due to the ligand-to-metal charge transfer (LMCT) $O^{2-} \rightarrow Mo^{6+}$ [58–60]. Different types of Mo oxide species can be found in the supported Mo catalysts, namely, polymolybdate Mo^{6+}oxide species and small MoO_3 clusters and crystallites in which Mo has an octahedral coordination sphere (O_h) and isolated tetrahedrally-coordinated molybdates $Mo^{6+}(T_d)$. All of them generally absorb at wavelengths between 220 and 330 nm [61]. Furthermore, the exact position of the absorption bands and/or energy

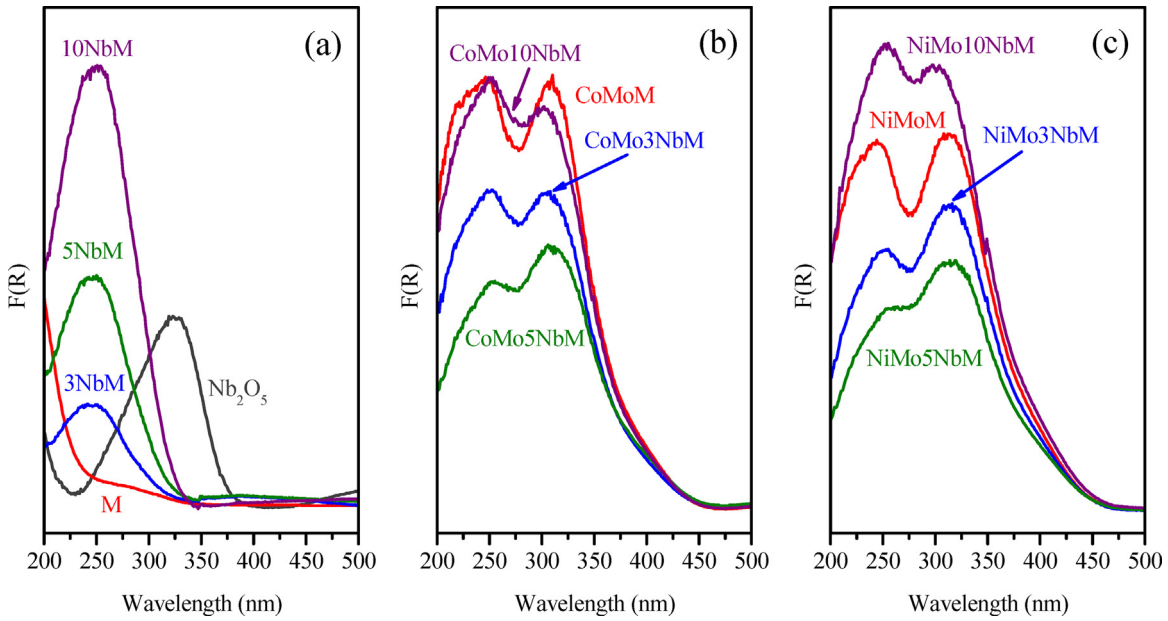

Fig. 5. UV–vis DR spectra of the *x*NbM supports (a), CoMo*x*NbM (b) and NiMo*x*NbM (c) catalysts, where *x* represents Nb loading in the supports (0, 3, 5 and 10 wt.%). The spectrum of the bulk Nb_2O_5 obtained after the calcination of ammonium niobate(V) oxalate hydrate at 500 °C for 4 h is also included in (a).

band gap (E_g) indicate the coordination and agglomeration degree of the Mo species in the sample [61].

The UV–vis DRS results obtained for the synthesized CoMo and NiMo catalysts are shown in Fig. 5(b and c). Broad absorption signals formed by two principal overlapped bands can be seen in the spectra of all catalysts. The first band is located at 250 nm for the CoMo catalysts and at 260 nm for the NiMo ones. The second band is situated at about 330 nm in both the CoMo and NiMo catalysts. In order to clarify which is the metal species that each of the above-described absorption signals can be attributed to UV–vis DR spectra of monometallic Co, Ni and Mo catalysts supported on M and *x*NbM materials were collected (Fig. S3). A comparison of the spectra of mono- and bimetallic catalysts showed that the first signal with the maximum at 250–260 nm could be ascribed to an electronic transition with $O^{2-} \rightarrow Ni^{2+}$ [62] or $O^{2-} \rightarrow Co^{2+}$ [63,64] charge transfer of octahedrally-coordinated Ni or Co oxide species (small NiO or CoO clusters). A low-intensity shoulder, which can be appreciated in the visible region of the spectra of the NiMo and CoMo catalysts (at about 400–420 nm wavelength) confirms the octahedral coordination of the Ni and Co oxide species and is attributed to their d–d electronic transitions. On the other hand, it is known that tetrahedrally-coordinated Mo oxide species (such as $[MoO_4]^{2-}$ and $[Mo_2O_7]^{2-}$) and low-polymerized octahedrally-coordinated Mo^{6+} oxide species also present absorption in the wavelength interval of 250–280 nm [58–61]. Therefore, our catalysts can also have some of the above-mentioned Mo species. The second signal observed in all spectra shown in Fig. 5 can be unambiguously assigned to the presence of agglomerated octahedrally-coordinated Mo oxide species (such as small MoO_3 clusters or agglomerated polymolybdates). The incorporation of niobium oxide into the MCM-41 support did not produce a noticeable change in the type of the deposited Ni, Co or Mo oxide species in the catalysts, nor in the calculated band gap energy (E_g), which was 3.4 eV for all cases.

3.1.7. Temperature-programmed reduction

Fig. 6 shows the reduction profiles of the synthesized CoMo and NiMo catalysts. Table 4 shows the corresponding H_2 consumptions and the total degree of reduction of the catalysts. The TPR profiles obtained for the catalysts of the CoMo and NiMo series have a similar shape (Fig. 6a and b, respectively): one well-defined intense reduction signal at a low-temperature region (200–600 °C, Zone I) of the thermograms and broad low-intensity hydrogen consumption at a high temperature interval (600–1000 °C, Zone II). The first intense H_2 consumption peak was located at about 507–517 °C for the CoMoM and CoMo*x*NbM catalysts and at a slightly lower temperature of about 412–436 °C for the NiMoM and NoMo*x*NbM catalysts. This low-temperature reduction peak can be assigned to the first step of reduction ($Mo^{6+} \rightarrow Mo^{4+}$) of octahedral Mo oxide species, $Mo^{6+}(O_h)$, probably of the agglomerated polymolybdate species or small MoO_3 crystals, detected by WA-XRD (Fig. 2b and c) and UV–vis DRS (Fig. 5b and c). According to the literature [65–67], CoO and NiO species in the Co/MCM-41 and Ni/MCM-41 catalysts can also be reduced in a single reduction step (from Co^{2+} to Co^0 [65] and from Ni^{2+} to Ni^0 [65–67]) at the same temperature interval (between 300 and 600 °C), being NiO easier to be reduced than the CoO. The hydrogen consumption at the high temperature zone (Zone II) can be associated with the second step of reduction (from Mo^{4+} to Mo^0) of polymeric octahedral Mo oxide species and

Table 4
Reduction behavior of CoMo and NiMo catalysts determined from the TPR results and f_{Mo} fraction for the corresponding sulfided catalysts estimated from the HRTEM results.

Sample [a]	H_2 consumption (mmol/g) [b]			α_R [c]	f_{Mo} [d]
	200–600 °C	600–1000 °C	Total		
CoMoM	1.87	0.68	2.56	0.72	0.26
CoMo3NbM	2.12	0.47	2.60	0.74	0.28
CoMo5NbM	2.19	0.40	2.58	0.73	0.26
CoMo10NbM	1.86	0.42	2.28	0.65	0.23
NiMoM	2.09	0.60	2.68	0.76	0.22
NiMo3NbM	2.35	0.40	2.75	0.78	0.26
NiMo5NbM	2.62	0.29	2.91	0.82	0.24
NiMo10NbM	2.32	0.32	2.64	0.75	0.23

[a] CoMo*x*NbM = CoMo*x*Nb/MCM-41; NiMo*x*NbM = NiMo*x*Nb/MCM-41; *x* = 0, 3, 5 and 10 wt.%.
[b] Hydrogen consumption determined from the TPR results.
[c] α_R, degree of the reduction of Co (or Ni) and Mo oxide species determined from the total H_2 consumption of each sample and the theoretical value corresponding to their complete reduction (3.50 mmol/g).
[d] f_{Mo}, fraction of Mo atoms on the edge surface (catalytically active surface) of MoS_2 particles estimated using Eqs. (1)–(3).

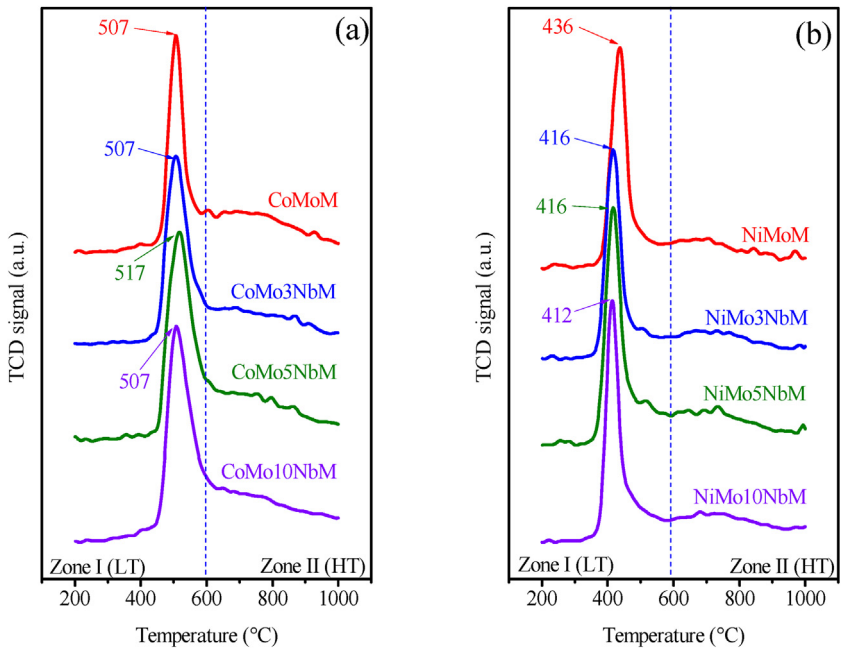

Fig. 6. TPR profiles of the catalysts: (a) CoMo*x*NbM and (b) NiMo*x*NbM, where *x* represents Nb loading in the supports (0, 3, 5 and 10 wt.%).

with the first step of reduction of isolated tetrahedral Mo species ($Mo^{6+}(T_d)$) in strong interaction with the silica support [68,69]. The broadness of the signal observed in Zone II indicates the coexistence of Mo oxide species with different degrees of agglomeration and coordination.

The incorporation of different amounts of Nb(V) oxide into the mesoporous MCM-41 supports did not result in a significant change in the TPR profiles of the CoMo and NiMo catalysts (Fig. 6). For the CoMo*x*NbM catalysts, an increase in the Nb loading in the support almost did not affect the position of the main reduction peak (507 °C), whereas for the NiMo*x*NbM catalysts, it produced a slight decrease in the temperature of reduction of octahedral Mo oxide species (from 436 to 412 °C). In the last case, it seems that the incorporation of Nb in the catalysts makes easier the reduction of the deposited Mo oxide species, which can be attributed to an increase in their dispersion on the Nb-containing supports. A more detailed analysis of the effect of Nb on the reduction behavior of the synthesized CoMo*x*NbM and NiMo*x*NbM catalysts revealed that the presence of Nb in the MCM-41 supports resulted in an increase in the H_2 consumption at a low temperature interval (Zone I) and a decrease at a high temperature interval (Zone II, Table 4). This effect was more pronounced for the catalysts of the NiMo series than for the CoMo ones. Finally, it should be mentioned that in contrast to the previously published work [70], we did not detect any reduction signal that can be attributed to the reduction of the Nb(V) oxide species in the TPR profiles of the *x*NbM supports (not shown) and *x*NbM-supported catalysts.

3.2. Characterization of sulfided catalysts

3.2.1. High resolution transmission electron microscopy

HRTEM is the most effective technique for the examination of the morphology of sulfide active phases, since it allows visualization of MoS_2 crystallite slabs on the support's surface. In the HRTEM micrographs of all characterized CoMo and NiMo catalysts (supported on pure silica MCM-41 or on Nb-containing materials), crystallites with the typical layered structure with interplanar distances of about 6.2 Å were observed (Fig. 7). These structures can be ascribed to the MoS_2 active phase particles with the 6.1 Å interlayer distances. It can be observed in Fig. 7 that the addition of 3 wt.% of Nb to the MCM-41 resulted in some changes in the dispersion of the MoS_2 particles. Previously, it was reported that the sulfided niobium species, NbS_2, have a crystallographic structure similar to that of the MoS_2, but with a slightly larger interplanar distance (6.3 Å). However, the formation of such sulfided NbS_2 phase is not possible in the case of our catalysts because it forms at a high temperature (about 950 °C followed by quenching from an annealing temperature of 750 °C) [71].

Fig. 8 shows the length (*L*) and stacking number (*N*) distributions of MoS_2 slabs in the sulfide NiMo and CoMo catalysts. Both length and stacking distributions are broader for the CoMoM and NiMoM catalysts supported on the Nb-free MCM-41 material than for the *x*NbM-supported counterparts. Therefore, the presence of Nb in the mesoporous MCM-41 supports resulted in more narrow distributions in the crystal length and stacking degree of the MoS_2 particles. The average length and stacking numbers of the MoS_2 crystallites calculated from the statistical analysis for the sulfided NiMo and CoMo catalysts are also shown in Fig. 8. It can be observed that the average crystallite size of the MoS_2 phase in the NiMo catalysts decreased from 54 to 46 Å after the addition of 3 wt.% of Nb in the MCM-41 support, whereas for the similar CoMo catalysts this decrease was from 45 to 42 Å. Regarding the average stacking degree, for the majority of the catalysts, Nb addition to the MCM-41 support also resulted in a decrease in the average stacking of MoS_2 slabs. The average values of *L* and *N* were used to estimate the fraction of Mo atoms on the catalytically active surface of the MoS_2 particles (f_{Mo} fraction). Table 4 shows the calculated f_{Mo} values. These values also confirm an increase in the proportion of Mo atoms available for the interaction with the reactant molecules in the CoMo and NiMo catalysts supported on *x*NbM, especially at low Nb loadings (3–5 wt.%), in comparison with the corresponding catalysts supported on MCM-41 silica. Therefore, it can be concluded that the addition of a small amount of Nb (around 3 wt.%) to MCM-41 is beneficial for the dispersion of the sulfided NiMo and CoMo catalysts.

3.3. Dibenzothiophene hydrodesulfurization reaction

Scheme 1 shows the mechanism of hydrodesulfurization (HDS) of dibenzothiophene (DBT), which occurs through two parallel

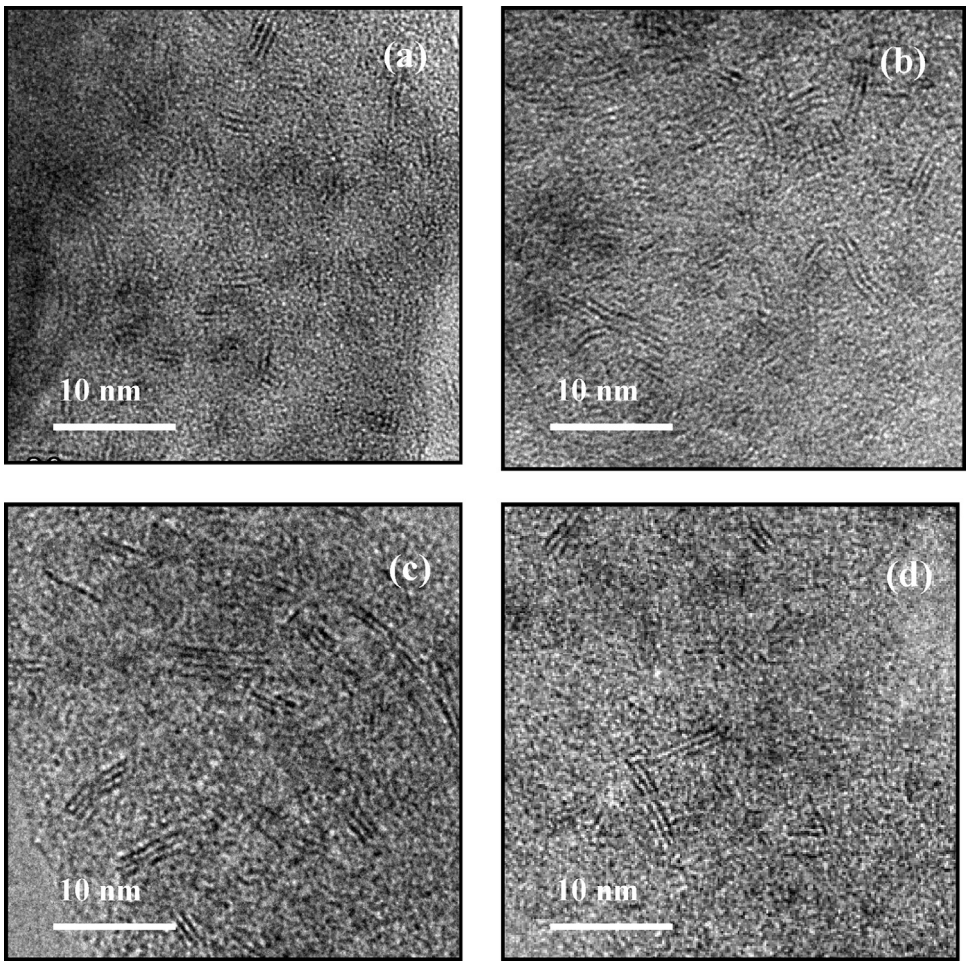

Fig. 7. HRTEM micrographs of selected sulfided catalysts: (a) CoMoM, (b) CoMo3NbM, (c) NiMoM and (d) NiMo3NbM.

reaction routes. The first pathway is called the direct desulfurization (DDS) and comprises the direct elimination of the S atom from the dibenzothiophene molecule via C-S bond cleavage, yielding biphenyl (BP). The second route is the hydrogenation (HYD) pathway, which consists of two steps: partial hydrogenation of one of the benzene rings of DBT, followed by the hydrogenolysis of the C-S bond and sulfur elimination. This pathway yields first tetrahydrodibenzothiophene (THDBT) and then the corresponding cyclohexylbenzene product (CHB). The latter can suffer further hydrogenation, leading to the formation of dicyclohexyl (DCH) (not shown in Scheme 1). At high DBT conversion, the possibility of further hydrogenation of the BP product to CHB also exists. The ratio between the two reaction pathways depends on both, the nature of the S-containing molecule and the catalyst [72].

In the present work, synthesized NiMo and CoMo catalysts were first sulfided *ex situ* and then tested in the DBT HDS reaction. Results obtained with the pure silica MCM-41 support and with the Nb-containing MCM-41 materials were compared to observe the effect of Nb on the catalytic performance of the NiMo and CoMo catalysts.

Table 5 shows the DBT conversions obtained with different catalysts at different reaction times (2, 4 and 8 h) and product distributions obtained at two DBT conversion values (40 and 80%). The DBT conversions obtained with the CoMo catalysts at 8 h reaction time changed in the following order: CoMo3NbM > CoMo5NbM > CoMo10NbM ≈ CoMoM. For the NiMo catalysts, the order was: NiMo3NbM > NiMo5NbM ≈ NiMo10NbM > NiMoM, respectively. In both cases, Nb-containing catalysts resulted to be more active than catalysts not containing Nb. The main desulfurized reaction products were biphenyl and cyclohexylbenzene. For the NiMo series catalysts, considerable amounts of the THDBT intermediate were also detected at low (40%) DBT conversion. At high DBT conversion (80%), traces of DCH were found for the NiMo catalysts, whereas for the CoMo ones and the NiMo10NbM sample, undesirable cracking products (benzene and cyclohexane) were formed in small amounts (below 2.4%). The relative amounts of the obtained products depended on the promoter (Co or Ni) used and on the support's Nb loading (Table 5). As expected, the DDS product (BP) was formed in a larger proportion with the CoMo catalysts, while the products of the HYD route (THDBT + CHB + DCH) were predominantly formed with the NiMo catalysts. This result is in good agreement with previous literature reports for $CoMo/Al_2O_3$ [73] and $NiMo/Al_2O_3$ [74] catalysts.

A more detailed analysis of the catalysts' selectivity and the effect of Nb on the reaction routes was made on the basis of the calculated rate constants shown in Table 6. The obtained overall pseudo-first-order rate constants' values (k) varied in a wide range, from 1.07×10^{-5} to 2.34×10^{-5} L/(s·g_{cat}). Among the CoMo*x*NbM catalysts, the most active samples were the CoMo3NbM and CoMo5NbM: both presented the rate constant k equal to 1.98×10^{-5} L/(s·g_{cat}). The activity of these two catalysts was about 1.5 times higher than that of the corresponding CoMoM sample without Nb. For the NiMo catalysts, Nb addition to the MCM-41 support also resulted in an increase of the activity. In this case, all Nb-containing catalysts showed higher k values than the reference NiMoM sample. The NiMo3NbM catalyst resulted to be the most active among all catalysts prepared in the present work.

Table 5
Catalytic performance of the synthesized catalysts in hydrodesulfurization of DBT.

Catalyst	DBT conversion (%)[a]			Product composition (%)[b]			Product composition (%)[c]			
	2 h	4 h	8 h	THDBT	BP	CHB	BP	CHB	DCH	B+CH
CoMoM	26	52	86	0.0	61.4	38.6	55.7	43.5	0.0	0.8
CoMo3NbM	35	67	98	0.0	70.2	29.8	66.1	32.9	0.0	1.0
CoMo5NbM	35	66	96	0.0	66.2	33.8	65.4	34.3	0.0	0.3
CoMo10NbM	22	45	87	0.0	61.6	38.4	56.2	43.0	0.0	0.8
NiMoM	28	52	88	8.8	42.2	49.0	37.6	59.6	2.8	0.0
NiMo3NbM	39	73	95	11.8	36.0	52.2	31.2	65.4	3.4	0.0
NiMo5NbM	33	68	93	12.8	34.4	52.8	29.4	67.4	3.2	0.0
NiMo10NbM	35	66	93	13.0	31.2	55.8	25.6	68.4	3.6	2.4

[a] At different reaction times.
[b] At 40% of DBT conversion. THDBT = tetrahydrodibenzothiophene; BP = biphenyl; CHB = cyclohexylbenzene.
[c] At 80% of DBT conversion. BP = biphenyl; CHB = cyclohexylbenzene; DCH = dicyclohexyl; cracking products: B = benzene and CH = cyclohexane.

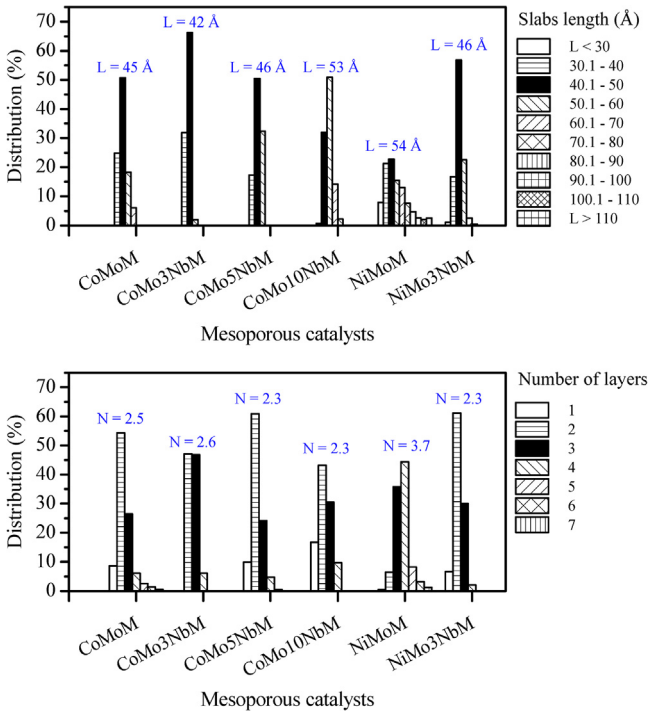

Fig. 8. Length (a) and stacking (b) distributions of MoS_2 crystallites in selected sulfided NiMo and CoMo catalysts. Average length (L) and average stacking number (N) of MoS_2 crystallites are shown for each catalyst.

Table 6
Apparent rate constants of CoMo and NiMo catalysts for HDS of DBT in the reaction network shown in Scheme 1.

Catalyst [a]	Rate constants, × 10^5 (L s^{-1} $g_{cat.}$) [b]					Ratio k_2^*/k_1^*
	k	k_1^*	k_2^*	k_3^*	k_4^*	
CoMoM	1.32	0.81	0.50	0.13	38.19	0.62
CoMo3NbM	1.98	1.37	0.61	0.06	42.57	0.44
CoMo5NbM	1.98	1.28	0.70	0.03	42.57	0.54
CoMo10NbM	1.07	0.67	0.40	0.11	38.19	0.60
NiMoM	1.38	0.61	0.78	0.23	23.65	1.28
NiMo3NbM	2.34	0.92	1.42	0.71	28.01	1.54
NiMo5NbM	2.09	0.74	1.35	0.52	25.99	1.68
NiMo10NbM	1.99	0.64	1.34	0.49	20.77	2.10

[a] CoMo*x*NbM = CoMo*x*Nb/MCM-41; NiMo*x*NbM = NiMo*x*Nb/MCM-41; x = 0, 3, 5 and 10 wt.%.
[b] k, overall pseudo-first-order rate constant; k_1^*, k_2^*, k_3^* and k_4^*–, apparent rate constants ($k_n^* = k_n K_n$, where k_n is the intrinsic kinetic rate constant and K_n is the equilibrium adsorption constant of each compound).

The value of k obtained with this catalyst (2.34×10^{-5} L/(s·g_{cat})) was 1.7 times higher than that of the similar catalyst without niobium (NiMoM).

From the above results, it can be concluded that the activity of the NiMo and CoMo catalysts supported on the *x*NbM materials passes through the maximum at niobium loadings about 3–5 wt.%. A further increase in the support's Nb loading to 10 wt.% resulted in a decrease in the activity of the CoMo*x*NbM and NiMo*x*NbM catalysts that can be attributed to a decrease in the dispersion of MoS_2 (f_{Mo} fraction, Table 4). In general, it can be seen that both the overall pseudo-first-order rate constants (k) of the NiMo and CoMo catalysts (Table 6) and the corresponding f_{Mo} fractions (Table 4) follow similar trends with Nb loading in the MCM-41 supports. Catalysts with larger f_{Mo} fractions show higher k values. However, the magnitude of the changes in the k and the f_{Mo} values was different. For example, the addition of 3 wt.% of Nb to the MCM-41 support produced an increase of k in 1.5–1.7 times for the CoMo and NiMo catalysts, respectively, whereas the f_{Mo} fraction increased in less than 10 %. Therefore, the effect of niobium in these catalysts is not limited to improving MoS_2 dispersion. There should be another reason for such a strong increase in the HDS activity of the sulfide NiMo and CoMo catalysts supported on Nb-containing MCM-41 materials. Further investigation is now in progress to clarify this point.

Table 6 shows also the apparent rate constants k_1^*, k_2^*, k_3^* and $-k_4^*$, which were calculated based on the kinetic model proposed by H. Farag [42,43] for the reaction network shown in Scheme 1. In this approach, the existence of two different kinds of catalytic active sites of (i) hydrogenation (HYD) and (ii) direct desulfurization (DDS) is assumed. The total rate can be expressed as $R_{Total} = R_{HYD} + R_{DDS}$ and the overall pseudo-first-order rate constant (k) is related to the apparent constants k_1^* and k_2^* as $k = k_1^* + k_2^* = k_1K_1 + k_2K_2$, where k_1 and k_2 are the intrinsic kinetic rate constants for the DDS and HYD routes, and K_1 and K_2 are the equilibrium adsorption constants of DBT over the catalytic active sites for DDS and HYD, respectively. Therefore, the k_2^*/k_1^* ratio characterizes the ability of each catalyst for the HYD and DDS routes of the reaction. The apparent rate constants k_3^* and k_4^* are also related to the intrinsic kinetic rate constants k_3 and k_4 and the equilibrium adsorption constants of BP and THDBT (K_3 and K_4, respectively) as $k_n^* = k_n K_n$. According to Scheme 1, k_1^* and k_4^* rate constants are related to hydrogenolysis reactions (C-S bond cleavage), whereas k_2^* and k_3^* constants correspond to the hydrogenation of DBT and BP, respectively. As it can be observed in Table 6, the CoMo*x*NbM catalysts had higher values of the k_1^* and k_4^* rate constants than the corresponding NiMo*x*NbM catalysts, which is in line with the high ability of the CoMo catalysts for hydrogenolysis reactions. On the contrary, the NiMo*x*NbM catalysts showed higher values of the k_2^* and k_3^* constants of hydrogenation reactions than the CoMo*x*NbM ones. The effect of the addition of 3–5 wt.% of Nb in the supports consisted in

an increase of all apparent rate constants, with the only exception of k_3* of the CoMo series catalysts. In the case of the CoMo catalysts, the apparent constant k_1* corresponding to the DDS pathway of the HDS reaction suffered a larger increase with the addition of 3–5 wt.% of Nb than the k_2* and k_4* constants related to hydrogenation. As a result, Nb-containing CoMo3NbM and CoMo5NbM catalysts showed lower k_2*/k_1* values than the reference CoNoM sample without Nb, which means that the addition of Nb to the silica support produced an increase in the CoMo catalysts' selectivity towards the direct desulfurization of DBT. On the contrary, for the NiMo*x*NbM catalysts, the k_2* and k_3* constants increased more after the addition of Nb to the supports. An increase in the k_1* value was less strong leading to an increase in the k_2*/k_1* ratio for the Nb-containing catalysts in comparison with the NiMoM sample. In this case, Nb loading to the MCM-41 supports resulted in an increase in the hydrogenation ability of the NiMo catalysts.

Resuming the above catalytic results, it can be concluded that the addition of small amounts of Nb (3–5 wt.%) to the MCM-41 supports had a positive effect on both catalytic activity and selectivity of the prepared catalysts. For the CoMo catalysts, Nb addition improved catalysts' selectivity towards the DDS pathway of the reaction, whereas for the NiMo catalysts, Nb addition increased their selectivity to hydrogenation. A more detailed study is needed to explain the reasons for these changes in activity and selectivity. A few researchers suggested previously that an increase in the HYD activity of the catalysts can be attributed to an increase in the acidic environment of the support, which affects the electron-deficient character of the active metal, favoring the adsorption of aromatic compounds and their hydrogenation [75,76]. However, the different effect of Nb on the selectivity of the CoMo and NiMo catalysts points out to the importance of not only the acidic properties of the support, but also the promoter's nature.

4. Conclusions

CoMo and NiMo catalysts supported on pure silica MCM-41 and on Nb-containing MCM-41 materials with different Nb loadings were prepared and tested in the hydrodesulfurization of dibenzothiophene. Characterization of the Nb-containing MCM-41 supports by Raman and XPS showed that only Nb(V) oxide species were present in them. These species were highly dispersed at low Nb loadings (3–5 wt.%) and existed as Nb oxide grafted to the surface silanol groups of the MCM-41 material. At high Nb loading (10 wt.%), in addition to the grafted Nb species, some agglomerated Nb_2O_5 species were detected as clusters or small crystals by Raman but were not detectable by XRD. CoMo and NiMo catalysts supported on 3NbM and 5NbM materials with well-dispersed grafted Nb oxide species showed higher catalytic activity than the corresponding CoMo and NiMo catalysts supported on MCM-41 silica. Selectivity of these catalysts was also affected by the addition of Nb, namely the CoMo catalysts increased their selectivity towards the DDS route of DBT hydrodesulfurization, while the NiMo catalysts became more selective for the HYD route of the reaction. This behavior could be due to the promoter's nature. However, it can be stated that the addition of Nb imptoved the activity and the characteristic selectivity of both CoMo and NiMo catalysts. This was confirmed by the calculated overall pseudo-first-order rate constant and the apparent rate constants for different steps of the DBT reaction network. Nevertheless, a more detailed study and characterization of the sulfided CoMo and NiMo catalysts supported on the Nb-containing MCM-41 materials is required to explain the reasons for the strong modifications in the catalytic activity and selectivity. On the other hand, a further increase in the supports' Nb loading to 10 wt.% resulted in some agglomeration of the deposited Nb_2O_5 species that leads to a decrease in the support's textural properties, worse dispersion of the sulfided MoS_2 species and lower catalytic activity.

Acknowledgments

F.J. Méndez acknowledges DGAPA-UNAM for the postdoctoral grant. This work was supported by DGAPA-UNAM, México (grant number IN-113715) and Consejo Nacional de Ciencia y Tecnología (CONACYT), México (grant number CB-220175). The authors thank C. Salcedo Luna, A. Morales Espino, I. Puente Lee and R. Ruiz Trejo for technical assistance.

Appendix A. Supplementary data

Supplementary data associated with this article can be found, in the online version, at http://dx.doi.org/10.1016/j.apcatb.2017.07.079.

References

[1] K.G. Knudsen, B.H. Cooper, H. Topsøe, Appl. Catal. A 189 (1999) 205–215.
[2] C. Song, Catal. Today 86 (2003) 211–263.
[3] Y. Yoshimura, M. Toba, H. Farag, K. Sakanishi, Catal. Surv. Asia 8 (2004) 47–60.
[4] M.L. Vrinat, Appl. Catal. 6 (1983) 137–158.
[5] P.T. Vasudevan, J.L.G. Fierro, Catal. Rev. 38 (1996) 161–188.
[6] H. Topsøe, B.S. Clausen, F.E. Massoth, Hydrotreating Catalysis: Science and Technology, Springer-Verlag, Berlin, 1996.
[7] J.S. Beck, J.C. Vartuli, W.J. Roth, M.E. Leonowicz, C.T. Kresge, K.D. Schmitt, C.T.W. Chu, D.H. Olson, E.W. Sheppard, J. Am. Chem. Soc. 114 (1992) 10834–10843.
[8] A. Wang, Y. Wang, T. Kabe, Y. Chen, A. Ishihara, W. Qian, J. Catal. 199 (2001) 19–29.
[9] A. Wang, Y. Wang, T. Kabe, Y. Chen, A. Ishihara, W. Qian, P. Yao, J. Catal. 210 (2002) 319–327.
[10] T.E. Klimova, M. Calderón, J. Ramıírez, Appl. Catal. A 240 (2003) 29–40.
[11] X. Li, A. Wang, Z. Sun, C. Li, J. Ren, B. Zhao, Y. Wang, Y. Chen, Y. Hu, Appl. Catal. A 254 (2003) 319–326.
[12] U.T. Turaga, C. Song, Catal. Today 86 (2003) 129–140.
[13] J.R. Grzechowiak, K. Mrozińska, A. Masalska, J. Góralski, J. Rynkowski, W. Tylus, Catal. Today 114 (2006) 272–280.
[14] M.J.B. Souza, B.A. Marinkovic, P.M. Jardim, A.S. Araujo, A.M.G. Pedrosa, R.R. Souza, Appl. Catal. A 316 (2007) 212–218.
[15] T. Chiranjeevi, G.M. Kumaran, G.M. Dhar, Petrol. Sci. Tech. 26 (2008) 690–703.
[16] E. Rodríguez-Castellón, A. Jiménez-López, D. Eliche-Quesada, Fuel 87 (2008) 1195–1206.
[17] S.J. Sardhar Basha, P. Vijayan, C. Suresh, D. Santhanaraj, K. Shanthi, Ind. Eng. Chem. Res. 48 (2009) 2774–2780.
[18] F.J. Méndez, E. Bastardo-González, P. Betancourt, L. Paiva, J.L. Brito, Catal. Today 143 (2013) 93–100.
[19] M. Ziolek, Catal. Today 78 (2003) 47–64.
[20] M. Ziolek, I. Sobczak, I. Nowak, P. Decyk, A. Lewandowska, J. Kujawa, Micropor. Mesopor. Mat. 35–36 (2000) 195–207.
[21] I.E. Wachs, J.M. Jehng, G. Deo, H. Hu, N. Arora, Catal. Today 28 (1996) 199–205.
[22] F.B. Noronha, D.A.G. Aranda, A.P. Ordine, M. Schmal, Catal. Today 57 (2000) 275–282.
[23] P. Chagas, H.S. Oliveira, R. Mambrini, M. Le Hyaric, M.V. de Almeida, L.C.A. Oliveira, Appl. Catal. A 454 (2013) 88–92.
[24] J.M.R. Gallo, I.S. Paulino, U. Schuchardt, Stud. Surf. Sci. Catal. 154C (2004) 2945–2950.
[25] C. Tiozzo, C. Bisio, F. Carniato, A. Gallo, S.L. Scott, R. Psaro, M. Guidotti, Phys. Chem. Chem. Phys. 15 (2013) 13354–13362.
[26] T. Iizuka, Y. Tanaka, K. Tanabe, J. Mol. Catal. 17 (1982) 381–389.
[27] T. Mori, A. Miyamoto, N. Takahashi, M. Fukagaya, T. Hattori, Y. Murakami, J. Phys. Chem. 90 (1986) 5197–5201.
[28] G.C. Collazzo, D.S. Paz, S.L. Jahn, N.L.V. Carreño, E.L. Foletto, Lat. Am. Appl. Res. 42 (2012) 51–54.
[29] A.C. Faro Jr., A.C.B. dos Santos, Catal. Today 118 (2006) 402–409.
[30] N. Allali, A.M. Marie, M. Danot, C. Geantet, M. Breysse, J. Catal. 156 (1995) 279–289.
[31] C. Geantet, J. Afonso, M. Breysse, N. Allali, M. Danot, Catal. Today 28 (1996) 23–30.
[32] V. Gaborit, N. Allali, C. Geantet, M. Breysse, M. Vrinat, M. Danot, Catal. Today 57 (2000) 267–273.
[33] L. Cedeño-Caero, A.R. Romero, J. Ramirez, Catal. Today 78 (2003) 513–518.
[34] A.S. Rocha, A.C. Faro Jr., L. Oliviero, J. Van Gestel, F. Maugé, J. Catal. 252 (2007) 321–334.
[35] J.G. Weissman, Catal. Today 28 (1996) 159–166.
[36] M. Danot, J. Afonso, J.L. Portefaix, M. Breysse, T. des Courieres, Catal. Today 10 (1991) 629–643.

[37] R. Palcheva, L. Kaluža, L. Dimitrov, G. Tyuliev, G. Avdeev, K. Jirátová, A. Spojakina, Appl. Catal. A 520 (2016) 24–34.
[38] International Center for Diffraction Data, PCPDFWIN v.2.02. PDF-2 Data Base, Newtown Philadelphia, 1995.
[39] T.F. Hayden, J.A. Dumesic, J. Catal. 103 (1987) 366–384.
[40] E.J.M. Hensen, P.J. Kooyman, Y. van der Meer, A.M. van der Kraan, V.H.J. de Beer, J.A.R. van Veen, R.A. van Santen, J. Catal. 199 (2001) 224–235.
[41] S. Kasztelan, H. Toulhoat, J. Grimblot, J.P. Bonnelle, Appl. Catal. 13 (1984) 127–159.
[42] H. Farag, Energy & Fuels 20 (2006) 1815–1821.
[43] H. Farag, J. Colloid Interface Sci. 348 (2010) 219–226.
[44] B. Marler, U. Oberhagemann, S. Vortmann, H. Gies, Microporous. Mater. 6 (1996) 375–383.
[45] K.C. Souza, N.D.S. Mohallem, E.M.B. Sousa, J. Sol-Gel Sci. Technol. 53 (2010) 418–427.
[46] F.J. Méndez, A. Llanos, M. Echeverría, R. Jáuregui, Y. Villasana, Y. Díaz, G. Liendo-Polanco, M.A. Ramos-García, T. Zoltan, J.L. Brito, Fuel 110 (2013) 249–258.
[47] A. Galarneau, M. Nader, F. Guenneau, F. Di Renzo, A. Gedeon, J. Phys. Chem. C 111 (2007) 8268–8277.
[48] C.P. Guthrie, E.J. Reardon, J. Phys. Chem. A 112 (2008) 3386–3390.
[49] A.L.-T. Pham, D.L. Sedlak, F.M. Doyle, Appl. Catal. A 126 (2012) 258–264.
[50] R. Kumar-Rana, B. Viswanathan, Catal. Lett. 52 (1998) 25–29.
[51] J.M. Jehng, I.E. Wachs, Chem. Mater. 3 (1991) 100–107.
[52] T. Murayama, J. Chen, J. Hirata, K. Matsumoto, W. Ueda, Catal. Sci. Technol. 4 (2014) 4250–4257.
[53] G. Blasse, J. Sol. State Chem. 7 (1973) 169–171.
[54] C.J. Brinker, R.K. Brow, D.R. Tallant, R.J. Kirkpatrick, J. Non-Cryst. Solids 120 (1990) 26–33.
[55] W.-H. Zhang, J. Lu, B. Han, M. Li, J. Xiu, P. Ying, C. Li, Chem. Mater. 14 (2002) 3413–3421.
[56] NIST Standard Reference Database 20, Version 4.1. https://srdata.nist.gov/xps/.
[57] M. Ziolek, I. Sobczak, Catal. Today 285 (2017) 211–225.
[58] N. Giordano, J.C.J. Bart, A. Vaghi, A. Castellan, G. Martinotti, J. Catal. 36 (1975) 81–92.
[59] Z. Liu, Y. Chen, J. Catal. 177 (1998) 314–324.
[60] C.C. Williams, J.G. Ekerdt, J.M. Jehng, F.D. Hardcastle, A.M. Turek, I.E. Wachs, J. Phys. Chem. 95 (1991) 8781–8791.
[61] O.Y. Gutiérrez, T.E. Klimova, J. Catal. 281 (2011) 50–62.
[62] B. Scheffer, J.J. Heijeinga, J.A. Moulijn, J. Phys. Chem. 91 (1987) 4752–4759.
[63] Á. Szegedi, M. Popova, C. Minchev, J. Mater. Sci. 44 (2009) 6710.
[64] A.P. Katsoulidis, D.E. Petrakis, G.S. Armatas, P.N. Trikalitis, P.J. Pomonis, Micropor. Mesopor. Mater. 92 (2006) 71–80.
[65] D. Liu, W.N.E. Cheo, Y.W.Y. Lim, A. Borgna, R. Lau, Y. Yang, Catal. Today 154 (2010) 229–236.
[66] R. Wojcieszak, S. Monteverdi, M. Mercy, I. Nowak, M. Ziolek, M.M. Bettahar, Appl. Catal. A 268 (2004) 241–253.
[67] Y. Yang, S. Lim, G. Du, Y. Chen, D. Ciuparu, G.L. Haller, J. Phys. Chem. B 109 (2005) 13237–13246.
[68] R. López-Cordero, F.J. Gil-Llambias, A. López-Agudo, Appl. Catal. 74 (1991) 125–136.
[69] B.Y. Jibril, S. Ahmed, Catal. Commun. 7 (2006) 990–996.
[70] M. Ziolek, I. Sobczak, A. Lewandowska, I. Nowak, P. Decyk, M. Renn, B. Jankowska, Catal. Today 70 (2001) 169–181.
[71] W.G. Fisher, M.J. Sienko, Inorg. Chem. 19 (1980) 39–43.
[72] F. Bataille, J.-L. Lemberton, P. Michaud, G. Pérot, M. Vrinat, M. Lemaire, E. Schulz, M. Breysse, S. Kasztelan, J. Catal. 191 (2000) 409–422.
[73] M. Houalla, N.K. Nag, A.V. Sapre, D.H. Broderick, B.C. Gates, AIChE J. 24 (1978) 1015–1021.
[74] J. Cheng-Zhang, H. Bin-Yu, J. Jun Nan, S. Geng, X. Guo Li, X. Long Qu, Y. Lin Shi, Y. Ting Zhang, H. Guang Liu, Adv. Mater. Res. 781–784 (2013) 304–307.
[75] M. Breysse, M. Cattenot, V. Kougionas, J.C. Lavalley, F. Mauge, J.L. Portefaix, J.L. Zotin, J. Catal. 168 (1997) 143–153.
[76] O. Cairon, K. Thomas, A. Chambellan, T. Chevreau, Appl. Catal. A 238 (2003) 167–183.